IEEE Access
Multidisciplinary | Rapid Review | Open Access Journal

Received February 13, 2020, accepted February 29, 2020, date of publication March 9, 2020, date of current version March 18, 2020.

Digital Object Identifier 10.1109/ACCESS.2020.2979350

A Cascaded Topology and Control Method for Two-Phase Receivers of Dynamic Wireless Power Transfer Systems

JINHAI JIANG[1,3], ZHONGGANG LI[2], KAI SONG[1], (Senior Member, IEEE), BEIBEI SONG[1], SHUAI DONG[1], AND CHUNBO ZHU[1], (Member, IEEE)

[1]School of Electrical Engineering and Automation, Harbin Institute of Technology, Harbin 150001, China
[2]School of Instrumentation Science and Engineering, Harbin Institute of Technology, Harbin 150001, China
[3]Postdoctoral Mobile Station of Mechanical Engineering, Harbin Institute of Technology, Harbin 150001, China

Corresponding author: Kai Song (kaisong@hit.edu.cn)

This work was supported in part by the National Natural Science Foundation of China under Grant 51677032 and 51577034, in part by the Natural Science Foundation of Heilongjiang Province under Grant E2017045, and in part by the Harbin Science and Technology Innovation Talents Special Fund Project under Grant 2016RAQXJ002.

ABSTRACT In a dynamic wireless power transfer (DWPT) system for electric vehicles, bipolar transmitting rail is often implemented to improve the misalignment tolerance, but its constraint often lies in fluctuating output. This problem can be mitigated by applying two-phase receivers which, due to its structural characteristics in the impedance matching circuit, bring two new problems: limited range of impedance matching and low efficiency. This paper aims to tackle the two problems by introducing a cascaded topology and its control method. Firstly, the conventional topology of the two-phase receiver is thoroughly analyzed theoretically concerning impedance matching range and efficiency model. Secondly, a cascaded bridgeless rectifier-Buck (CBRB) as impedance matching with $0\sim\infty\Omega$ matching capabilities is put forward. Besides, the independent two-channel structure is also introduced leaving the output current ratio the key to efficiency optimization. Thirdly, the control method for the proposed topology using heuristic current ratio by adopting online estimation via auxiliary measurement coils is presented. Finally, experiments are verified on a 20 kW DWPT platform and the proposed topology and control method can raise the transfer efficiency by 3.3% compared with the conventional topology.

INDEX TERMS Cascaded bridgeless rectifier-Buck, heuristic current ratio, impedance matching, two-phase receivers, dynamic wireless power transfer.

I. INTRODUCTION

Electric vehicles (EVs) have been drawing attention in many fields recently due to the potential of environmental protection and substitution of fuel-based vehicles [1]. However, the most significant challenges impeding their popularization are the limited driving range, charging equipment, the size and the weight of the batteries and a series of safety concerns. Wireless power transfer (WPT) has been studied intensively in order to improve the charging process and solve the problems mentioned above [2]. Dynamic wireless power transfer (DWPT), as a case of WPT, is proposed expecting the achieve continuous charging to extend the driving range of EVs and lighten the bulky batteries [3]–[6].

The associate editor coordinating the review of this manuscript and approving it for publication was Tariq Masood.

According to the coils of power transmitter, DWPT systems can be divided into three types: long coil type [7]–[9], array coil type [10], [11] and bipolar type [12]–[14]. Bipolar power supply coil contains two contrary magnetic poles and the magnetic field lines above the transmitting coil extend along its laying direction (Fig. 1). Compared with the other two types, this bipolar type stands out for its numerous advantages such as high tolerance of misalignment, low magnetic flux leakage, and decent EMC. However, as the receiver moves along the bipolar rail, the mutual inductance of the coils varies in a wide range together with the load conditions. These varying parameters often lead to the fluctuation of the output power making it more difficult to achieve objectives such as constant current output. In addition, coupling zeros points occur when there is only one receiver implemented on the secondary side.

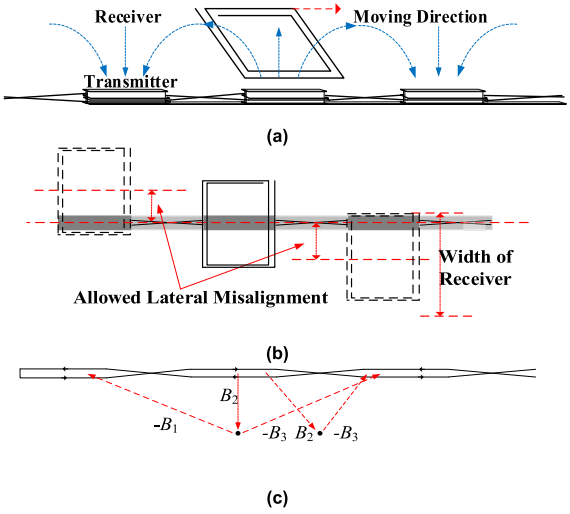

FIGURE 1. Diagram of bipolar type couplers (a) Distribution of magnetic field. (b) Sketch of lateral misalignment (c) Magnetic field distribution around power rail.

To deal with the fluctuating output power, recent researches focus on active impedance matching circuits, through which maximum power transmission and optimal efficiency can also be achieved [15]. Currently, active impedance matching topologies consist of various DC-DC converters [16]. Single-stage impedance matching for DWPT systems uses Buck or Boost circuits, and it works under either strongly coupled or loosely coupled conditions but not both. Multistage converters can usually achieve full-range impedance such as cascaded Buck-Boost topology, thus they are also extensively used. However, more stages of circuits lead to more power loss from the devices, which violates the goal of high-efficiency power transmission. Reference [17] presented a controlled rectifier that achieved impedance matching from AC to DC by controlling the conduction angle. It increases efficiency and minimizes the stages of the DC-DC converters to only one.

To deal with the coupling zero points when single-phase receivers are applied, one solution is adopting multiphase receivers on the secondary side because the mutual inductance of each receiving coil and transmitting coil are phase complimentary as their relative position varies. The effect of coupling zeros is shown in Fig. 2. Reference [18] proposed and analyzed multiphase receivers successfully reduced the output fluctuation by 50% in a 10kW experiment. However, when a multiphase receiver works with active impedance matching topology to suppress the fluctuation, the efficiency is low because it is difficult to tune the parameters of the two phases and have them work accordingly. The range of impedance matching also remains unexplored in such conditions.

This paper aims to explore the impedance matching topologies for two-phase receivers for the improvement of matching range and transfer efficiency. In Section II, this paper analyzes the impedance matching range and efficiency of the conventional topology for the two-phase receivers.

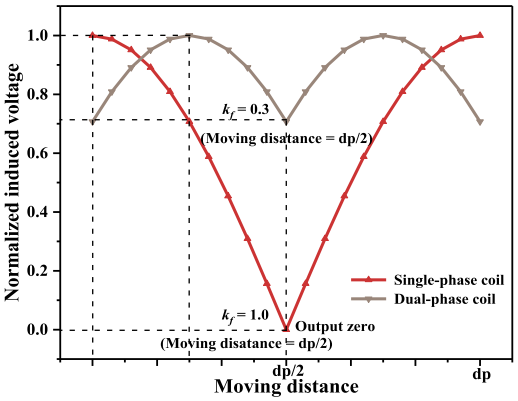

FIGURE 2. A demonstration of coupling zeros from [18] where k_f indicates the extent of fluctuation.

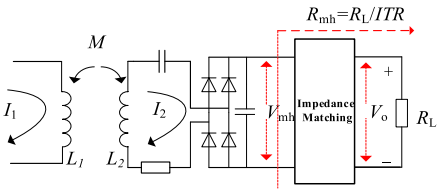

FIGURE 3. A general diagram impedance matching circuits.

In Section III, the proposed topology using independent two-channel structure combined with cascaded bridgeless rectifier-Buck (CBRB) is introduced and analyzed in detail to prove the improvement of the performance in theory. The control method for the proposed topology is put forward implementing on online current estimation with auxiliary measurement coils in Section IV. In Section V, 20-kW experiments provide solid proof of the effectiveness of the proposed topology and control method.

II. IMPEDANCE MATCHING AND EFFICIENCY MODEL FOR CONVENTIONAL TWO-PHASE RECEIVERS

A. CHARACTERISTICS OF IMPEDANCE TRANSFORMATION

In order to realize the constant current output of the secondary side, active impedance matching circuits are needed for the receiver [19], [20]. At present, the active impedance matching circuits generally consist of DC-DC converters, AC-DC converters or a combination of both. In order to simplify the analysis, the WPT system is generally modeled as the structure shown in Fig. 3, where V_{mh} is the input voltage of the impedance matching circuit and ITR is the impedance transformation ratio of the matching circuit.

If the impedance matching circuit is a Buck circuit and the components are all ideal, the relationship between the input voltage, output voltage, and duty cycle D is

$$V_{\mathrm{o}} = DV_{\mathrm{mh}} \tag{1}$$

Since all the devices in the circuit are ideal, the input power and output power of the circuit are equal:

$$\frac{V_{\mathrm{o}}^2}{R_{\mathrm{L}}} = \frac{V_{\mathrm{mh}}^2}{R_{\mathrm{mh}}} \tag{2}$$

Then the impedance transformation ratio of the Buck circuit is written as:

$$ITR = \frac{R_{\mathrm{L}}}{R_{\mathrm{mh}}} = \frac{V_{\mathrm{o}}^2}{V_{\mathrm{mh}}^2} = \frac{1}{D^2} \tag{3}$$

Assuming the WPT is in the resonant state, the output current can be deduced as

$$I_{\mathrm{o}} = \frac{\omega_0 M I_1}{\frac{2R_{\mathrm{L}}}{\pi}\sqrt{\frac{2}{ITR}}} \tag{4}$$

where ω_0 is the resonance frequency of the system. Equation (4) shows when I_1, M and the R_{L} are constant, the output current can be adjusted only by tuning ITR. On the other hand, tuning ITR can also maintain constant output if the parameters vary.

In DWPT systems powered through bipolar transmitters, parameters such as M and equivalent load fluctuate drastically because of the versatile loads on the vehicle and complex and varying working conditions. As such, the range of impedance matching should be as large as possible. Common DC-DC converters are widely used for active impedance matching including the six basic forms: Buck, Boost, Buck-boost, Cuk, SEPIC (Single Ended Primary Inductor Converter), and Zeta. Their characteristics are summarized in TABLE 1, where we discover that the transformation range of Buck and Boost is limited, the input and output polarity of Cuk is reversed, and the rest introduces more components entailed by more power loss.

TABLE 1. Basic characteristics of six kinds DC-DC converters.

Converter	Load voltage	Equivalent impedance R_{mh}	Transformation range
Buck	DV_{in}	$\frac{R_{\mathrm{L}}}{D^2}$	$R_{\mathrm{L}} \sim +\infty$
Boost	$\frac{1}{1-D}V_{\mathrm{in}}$	$(1-D)^2 R_{\mathrm{L}}$	$0 \sim R_{\mathrm{L}}$
Buck-Boost	$\frac{D}{1-D}V_{\mathrm{in}}$	$\frac{(1-D)^2}{D^2}R_{\mathrm{L}}$	$0 \sim +\infty$
Cuk, SEPIC, Zeta	$\frac{D}{1-D}V_{\mathrm{in}}$	$\frac{(1-D)^2}{D^2}R_{\mathrm{L}}$	$0 \sim +\infty$

B. EFFICIENCY MODEL OF TWO-PHASE RECEIVERS

A conventional structure of the two-phase receivers is shown in Fig. 4, where two groups of rectifiers in parallel are connected with a mutual impedance matching circuit with I_o being the total output current. Since the two-phases of the receiver work alternately, the impedance transformation ratio is also ITR.

Based on the relative positions Py between the transmitter and the receiver, the Phase A (labeled with subscript ph1) and Phase B (labeled with subscript ph2) work alternately, the induced voltage V_{ind} in the receiver is

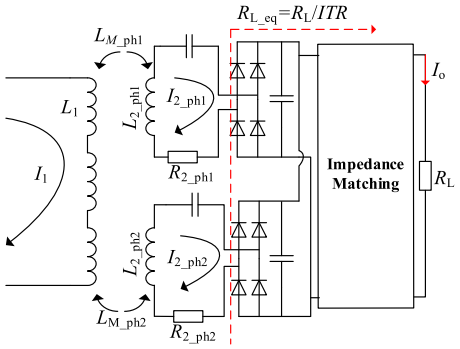

FIGURE 4. Conventional topology for two-phase receivers.

$$V_{ind} = \begin{cases} V_{\mathrm{ind\_ph1}} & \frac{\pi}{l}P_{\mathrm{y}} + \varphi_0 = \frac{\pi}{4} \sim \frac{3\pi}{4} \\ V_{\mathrm{ind\_ph2}} & \frac{\pi}{l}P_{\mathrm{y}} + \varphi_0 = \frac{3\pi}{4} \sim \frac{5\pi}{4} \end{cases} \tag{5}$$

Define impedance transformation ratio now as

$$ITR = \frac{R_{\mathrm{L}}}{R_{\mathrm{L\_eq}}} \tag{6}$$

The output current and the resonant cavity current can be expressed as

$$\frac{I_{\mathrm{o}}^2}{I_2^2} = \frac{1}{ITR} \tag{7}$$

which makes

$$I_2 = I_o\sqrt{ITR} = \frac{V_{\mathrm{ind}}}{\left(R_2 + \frac{R_{\mathrm{L}}}{ITR}\right)} \tag{8}$$

Since $R_{\mathrm{L\_eq}} \gg R_2$, the impedance transformation ratio can be approximately expressed as

$$ITR \approx \frac{I_{\mathrm{o}}^2 R_{\mathrm{L}}^2}{V_{\mathrm{ind}}^2} \tag{9}$$

When phase A coil of the system is working, the secondary resonant cavity current I_{2_ph1} is

$$\begin{aligned} I_{2\_\mathrm{ph1}} &= \sqrt{ITR_{\mathrm{ph1}}}I_{\mathrm{o}} = I_{\mathrm{o}}\frac{I_{\mathrm{o}}R_{\mathrm{L}}}{V_{\mathrm{ind\_ph1}}} \\ &= I_o\frac{I_{\mathrm{o}}R_{\mathrm{L}}}{\omega I_{\mathrm{p}}k_{1\max}\sqrt{L_1 L_{2\_\mathrm{ph1}}}}\frac{1}{\left|\sin(\frac{\pi}{l}P_{\mathrm{y}} + \varphi_0)\right|} \end{aligned} \tag{10}$$

When Phase B coil of the system is working, the secondary resonant cavity current I_{2_ph2} is

$$\begin{aligned} I_{2\_\mathrm{ph2}} &= \sqrt{ITR_{\mathrm{ph2}}}I_o = I_o\frac{I_{\mathrm{o}}R_{\mathrm{L}}}{V_{\mathrm{ind\_ph2}}} \\ &= I_o\frac{I_{\mathrm{o}}R_{\mathrm{L}}}{\omega I_{\mathrm{p}}k_{2\max}\sqrt{L_1 L_{2\_\mathrm{ph2}}}}\frac{1}{\left|\cos(\frac{\pi}{l}P_{\mathrm{y}} + \varphi_0)\right|} \end{aligned} \tag{11}$$

As the receiver runs an integer multiple of pole distance along the transmitter and maintains constant current output,

the RMS value of the current in the resonant cavity can be expressed as

$$\bar{I}_{2\_\mathrm{rms}} = I_o \frac{I_o R_\mathrm{L}}{\omega I_\mathrm{p} k_{1\max}\sqrt{L_1 L_{2\_\mathrm{ph1}}}} \times \sqrt{\frac{\int_{\frac{\pi}{4}+N\pi}^{\frac{3\pi}{4}+N\pi}\left(\frac{1}{|\sin(\frac{\pi}{l}P_\mathrm{y}+\varphi_0)|}\right)^2 \mathrm{d}(\frac{\pi}{l}P_\mathrm{y}+\varphi_0) + \int_{\frac{3\pi}{4}+N\pi}^{\frac{5\pi}{4}+N\pi}\left(\frac{1}{|\cos(\frac{\pi}{l}P_\mathrm{y}+\varphi_0)|}\right)^2 \mathrm{d}(\frac{\pi}{l}P_\mathrm{y}+\varphi_0)}{\pi}} = \sqrt{\frac{4}{\pi}} I_o \frac{I_o R_\mathrm{L}}{\omega I_\mathrm{p} k_{1\max}\sqrt{L_1 L_{2\_\mathrm{ph1}}}} \tag{12}$$

As such, we can calculate the average efficiency of the receiver as

$$\bar{\eta}_{\mathrm{S\_L}} = \frac{P_\mathrm{L}}{P_\mathrm{L} + P_{\mathrm{RS\_loss}}} = \frac{R_M}{R_\mathrm{L} + \frac{4}{\pi}\left(\frac{I_o^2 R_\mathrm{L}}{\omega I_\mathrm{p} k_{1\max}\sqrt{L_1 L_{2\_\mathrm{ph1}}}}\right)^2 R_2} \tag{13}$$

III. PROPOSED TOPOLOGY

A. CASCADED BRIDGELESS RECTIFIER-BUCK

The bridgeless rectifier circuit model is shown in Fig. 5, where the two diodes of the lower arms in a regular rectifier are replaced by high-frequency switching devices, such as MOSFET or IGBT. C_o is the capacitor of the output filter, R_mh is the equivalent impedance connected with the bridgeless rectifier, and U_rec is the output voltage of the bridgeless rectifier.

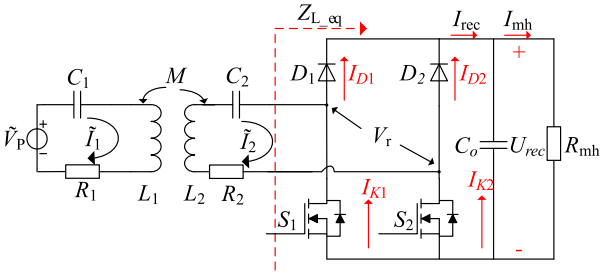

FIGURE 5. Circuitry of bridgeless rectifier.

The working mode and waveform of this kind of bridgeless rectifier are shown in Fig. 6 and Fig. 7, respectively. In order to simplify the analysis, assume that the devices used are ideal, the output filter capacity is large enough, and the system is resonant.

In Fig. 7, $\phi = \pi\,(t_2 - t_1)\,/\,(t_4 - t_0)$ is the conduction angle to the input voltage V_r of the rectifier, V_ind is the induced voltage in the receiver, and I_2 is the current in the resonant cavity. In a signal period, the input voltage V_r can

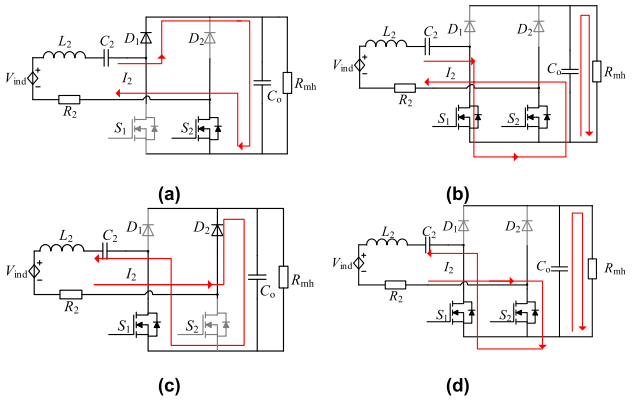

FIGURE 6. Working modes of bridgeless rectifier. (a) $V_r > 0$, S_1 off, S_2 on, D_1 on, D_2 off. (b) $V_r > 0$, S_1 on, S_2 off, D_1 off, D_2 off. (c) $V_r < 0$, S_1 on, S_2 off, D_1 off, D_2 on. (d) $V_r < 0$, S_1 off, S_2 on, D_1 off, D_2 off.

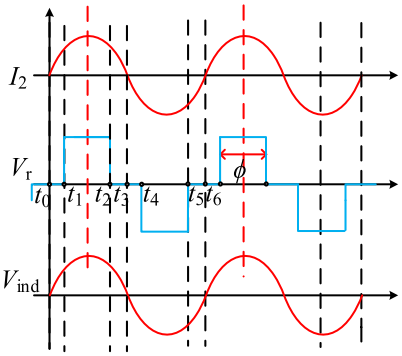

FIGURE 7. Ideal working waveforms of bridgeless rectifier.

be expressed as

$$V_\mathrm{r} = \begin{cases} 0 & 0 \le t \le t_1 \\ U_\mathrm{rec} & t_1 \le t \le t_2 \\ 0 & t_2 \le t \le t_4 \\ -U_\mathrm{rec} & t_4 \le t \le t_5 \\ 0 & t_5 \le t \le t_6 \end{cases} \tag{14}$$

According to the First Harmonic Approximation (FHA), the RMS value of the input voltage of the bridgeless rectifier can be derived as

$$V_{\mathrm{r\_rms}} = \frac{2\sqrt{2}U_\mathrm{rec}}{\pi}\sin(\frac{\phi}{2}) \tag{15}$$

The RMS value of the output current I_mh is

$$I_\mathrm{mh} = \frac{1}{\pi}\int_{\frac{\pi}{2}-\frac{\phi}{2}}^{\frac{\pi}{2}+\frac{\phi}{2}} \sqrt{2} I_{2\_\mathrm{rms}} \sin(\omega_0 t)\mathrm{d}\,(\omega_0 t) = \frac{2\sqrt{2}}{\pi} I_{2\_\mathrm{rms}} \sin(\frac{\phi}{2}) \tag{16}$$

By calculating the ratio of $V_{\mathrm{r\_rms}}$ to I_{2_rms}, the relationship between the input equivalent impedance and the load impedance is

$$R_{\mathrm{L\_eq}} = \frac{4}{\pi^2} R_\mathrm{mh}(1 - \cos(\phi)) \tag{17}$$

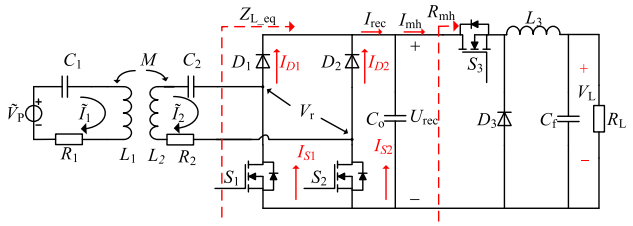

FIGURE 8. Cascaded bridgeless rectifier-Buck circuit.

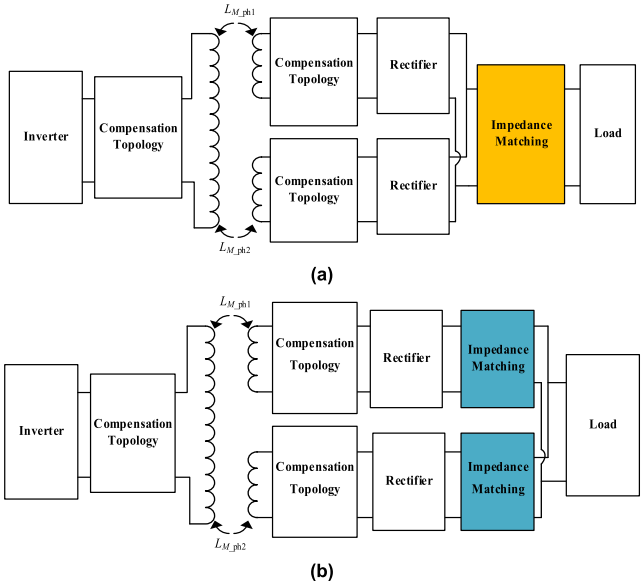

FIGURE 9. Diagram of two kinds of impedance matching structures for constant current output. (a) The conventional lumped impedance matching structure (b) The independent two-channel impedance matching structure.

The variation range of the conduction angle is $0\sim\pi$. When $\phi=\pi$, the working state of the bridgeless rectifier is the same as that of the uncontrolled rectifier, and the impedance relationship is

$$R_{\mathrm{L\_eq}}=\frac{8}{\pi^2}R_{\mathrm{mh}} \tag{18}$$

The transformation range of the bridgeless rectifier is $0\sim\frac{8}{\pi^2}R_{\mathrm{mh}}$ which is nearly from 0 to R_{mh}. According to TABLE 1, the transformation range of Buck is $R_{\mathrm{mh}}\sim+\infty$, so the overall transformation range of this cascaded circuit shown in Fig. 8 is approximately $0\sim+\infty$. Although other combinations of DC-DC converters can also achieve a full range of transformation, this topology reduces the impedance matching circuits to only one stage and requires fewer power-consuming components.

B. INDEPENDENT TWO-CHANNEL STRUCTURE OF IMPEDANCE MATCHING

For the two-phase receivers, two rectifiers are needed and connected in parallel. The outputs of the rectifiers are conventionally joined into one impedance matching module if needed for constant current output. The lumped structure of impedance matching is shown in Fig. 9(a) and the independent two-channel structure of impedance matching is shown in Fig. 9(b), respectively.

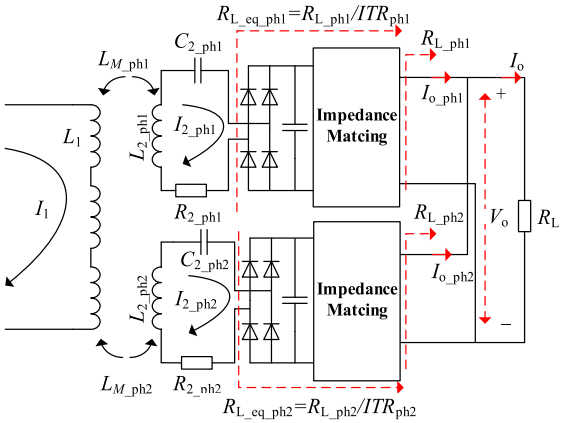

FIGURE 10. Circuitry of independent two-channel impedance matching structure.

In comparison with the efficiency of the lumped impedance matching for two-phase receivers in (13), the advantage of the independent structure is explained. Because the two groups of rectifiers and impedance matching circuits are connected in parallel, assume the total output current is I_{o}. In the analysis, assume that the system is in resonance state as in

$$\frac{1}{\sqrt{L_1C_1}}=\frac{1}{\sqrt{L_{2\_\mathrm{ph1}}C_{2\_\mathrm{ph1}}}}=\frac{1}{\sqrt{L_{2\_\mathrm{ph2}}C_{2\_\mathrm{ph2}}}}=2\pi f_0 \tag{19}$$

For convenience, components of Phase A and Phase B are labeled with subscript ph1 and ph2, respectively. Fig. 10 shows the circuitry of the independent impedance matching structure. Assume that the output current of the two-phase is independent in the ratio of $\kappa<1$ as in $I_{o\_ph1}=\kappa I_o$ and $I_{\mathrm{o\_ph2}}=(1-\kappa)I_{\mathrm{o}}$, and the impedance transformation ratios of the two phases are ITR_{ph1} and ITR_{ph2}. The currents of the resonant cavity can be expressed as

$$\begin{cases} I_{2\_\mathrm{ph1}}=\dfrac{I_{\mathrm{o\_ph1}}}{\sqrt{ITR_{\mathrm{ph1}}}}=\dfrac{\kappa I_o}{\sqrt{ITR_{\mathrm{ph1}}}} \\ I_{2\_\mathrm{ph2}}=\dfrac{I_{\mathrm{o\_ph2}}}{\sqrt{ITR_{\mathrm{ph2}}}}=\dfrac{(1-\kappa)I_{\mathrm{o}}}{\sqrt{ITR_{\mathrm{ph2}}}} \end{cases} \tag{20}$$

With the goal of constant total output current of the receiver and the assumption that all devices are ideal, the principle of constant power is

$$\begin{cases} V_{\mathrm{ind\_ph1}}I_{2\_\mathrm{ph1}}=\kappa I_{\mathrm{o}}\,(I_oR_{\mathrm{L}}) \\ V_{\mathrm{ind\_ph2}}I_{2\_\mathrm{ph2}}=(1-\kappa)\,I_{\mathrm{o}}\,(I_{\mathrm{o}}R_{\mathrm{L}}) \end{cases} \tag{21}$$

The currents in the resonant cavity and the transformation ratio of the two phases are

$$\begin{cases} I_{2\_\mathrm{ph1}}=\dfrac{\kappa I_{\mathrm{o}}^2R_{\mathrm{L}}}{\omega I_1k_{1\,\max}\sqrt{L_1L_{2\_\mathrm{ph1}}}\left|\sin(\frac{\pi}{l}P_{\mathrm{y}}+\varphi_0)\right|} \\ I_{2\_\mathrm{ph2}}=\dfrac{(1-\kappa)\,I_{\mathrm{o}}^2R_L}{\omega I_1k_{2\,\max}\sqrt{L_1L_{2\_\mathrm{ph2}}}\left|\cos(\frac{\pi}{l}P_{\mathrm{y}}+\varphi_0)\right|} \end{cases} \tag{22}$$

$$\begin{cases} ITR_{\text{ph1}} \approx \left(\dfrac{\omega I_1 k_{1\max} \left|\sin(\frac{\pi}{l}P_y + \varphi_0)\right| \sqrt{L_1 L_{2\_\text{ph1}}}}{R_L I_o} \right)^2 \\ ITR_{\text{ph2}} \approx \left(\dfrac{\omega I_1 k_{2\max} \left|\cos(\frac{\pi}{l}P_y + \varphi_0)\right| \sqrt{L_1 L_{2\_\text{ph2}}}}{R_L I_o} \right)^2 \end{cases} \tag{23}$$

Heuristically, set $\kappa = \sin^2(\frac{\pi}{l}P_y + \varphi_0)$ so that when the receiver moves an integer multiple of magnetic pole distances over the transmitter, the receiver coil currents are:

$$\begin{cases} I_{2\_\text{ph1}} = \dfrac{\kappa I_O^2 R_L}{\omega I_1 k_{1\max}\sqrt{L_1 L_{2\_\text{ph1}}}\left|\sin(\frac{\pi}{l}P_y + \varphi_0)\right|} \\ \quad = \dfrac{I_O^2 R_L}{\omega I_1 k_{1\max}\sqrt{L_1 L_{2\_\text{ph1}}}}\left|\sin(\dfrac{\pi}{l}P_y + \varphi_0)\right| \\ I_{2\_\text{ph2}} = \dfrac{(1-\kappa) I_O^2 R_L}{\omega I_1 k_{2\max}\sqrt{L_1 L_{2\_\text{ph2}}}\left|\cos(\frac{\pi}{l}P_y + \varphi_0)\right|} \\ \quad = \dfrac{I_O^2 R_L}{\omega I_1 k_{2\max}\sqrt{L_1 L_{2\_\text{ph2}}}}\left|\cos(\dfrac{\pi}{l}P_y + \varphi_0)\right| \end{cases} \tag{24}$$

Thus, the RMS values of the currents in the resonance cavity of the receiver can be computed:

$$\begin{cases} I_{2\_\text{ph1}\_rms} = \dfrac{I_O^2 R_L}{\omega I_1 k_{1\max}\sqrt{L_1 L_{2\_\text{ph1}}}} \\ \quad \sqrt{\dfrac{\int_0^{\pi}\left(\left|\sin(\frac{\pi}{l}P_y + \varphi_0)\right|\right)^2 \mathrm{d}\left(\frac{\pi}{l}P_y + \varphi_0\right)}{\pi}} \\ \quad = \dfrac{\sqrt{2}}{2}\dfrac{I_O^2 R_L}{\omega I_1 k_{1\max}\sqrt{L_1 L_{2\_\text{ph1}}}} \\ \bar{I}_{2\_\text{ph2}\_rms} = \dfrac{I_O^2 R_L}{\omega I_1 k_{2\max}\sqrt{L_1 L_{2\_\text{ph2}}}} \\ \quad \sqrt{\dfrac{\int_0^{\pi}\left(\left|\cos(\frac{\pi}{l}P_y + \varphi_0)\right|\right)^2 \mathrm{d}\left(\frac{\pi}{l}P_y + \varphi_0\right)}{\pi}} \\ \quad = \dfrac{\sqrt{2}}{2}\dfrac{I_O^2 R_L}{\omega I_1 k_{2\max}\sqrt{L_1 L_{2\_\text{ph2}}}} \end{cases} \tag{25}$$

Assume the same parameters of the two-phase coils:

$$\begin{cases} L_s = L_{2\_\text{ph1}} = L_{2\_\text{ph2}} \\ k_{\max} = k_{1\max} = k_{2\max} \\ R_2 = R_{2\_\text{ph1}} = R_{2\_\text{ph2}} \end{cases} \tag{26}$$

The average efficiency of the independent impedance matching structure of the two-phase receivers can be computed as

$$\begin{aligned} &\bar{\eta}_{\text{S\_I}} \\ &= \frac{P_L}{P_L + P_{\text{RS\_ph1\_loss}} + P_{\text{RS\_ph2\_loss}}} \\ &= \frac{R_M}{R_L + \left(\frac{\sqrt{2}}{2}\frac{I_O^2 R_L}{\omega I_1 k_{\max}\sqrt{L_1 L_s}}\right)^2 R_2 + \left(\frac{\sqrt{2}}{2}\frac{I_O^2 R_L}{\omega I_1 k_{\max}\sqrt{L_1 L_s}}\right)^2 R_2} \\ &= \frac{R_L}{R_L + \left(\frac{I_O^2 R_L}{\omega I_1 k_{\max}\sqrt{L_1 L_s}}\right)^2 R_2} \end{aligned} \tag{27}$$

The efficiency of the two impedance matching structures are compared as

$$\begin{aligned} \bar{\eta}_{\text{S\_I}} &= \frac{R_L}{R_L + \left(\frac{I_O^2 R_L}{\omega I_p k_{\max}\sqrt{L_1 L_{2\_\text{ph1}}}}\right)^2 R_2} > \bar{\eta}_{\text{S\_L}} \\ &= \frac{R_L}{R_L + \frac{4}{\pi}\left(\frac{I_O^2 R_L}{\omega I_p k_{1\max}\sqrt{L_1 L_{2\_\text{ph1}}}}\right)^2 R_2} \end{aligned} \tag{28}$$

The average efficiency of the independent two-channel impedance matching structure is higher than that of the conventional lumped structure. It should be noted that the current ratio is the key to efficiency improvement and this paper adopt a heuristic current ratio for explanation and deduction leaving space for future optimization.

IV. CONTROL METHOD USING ONLINE ESTIMATION

In order to achieve the current ratio $\kappa = \sin^2(\frac{\pi}{l}P_y + \varphi_0)$, it is necessary to implement auxiliary coils for an online estimation of some signals from the transmitter. The auxiliary measurement coil is wound closely to the two outermost coils of the receiver shown in Fig.11(a). Fig. 11(b) is the equivalent circuit model whose notations are listed in TABLE 2.

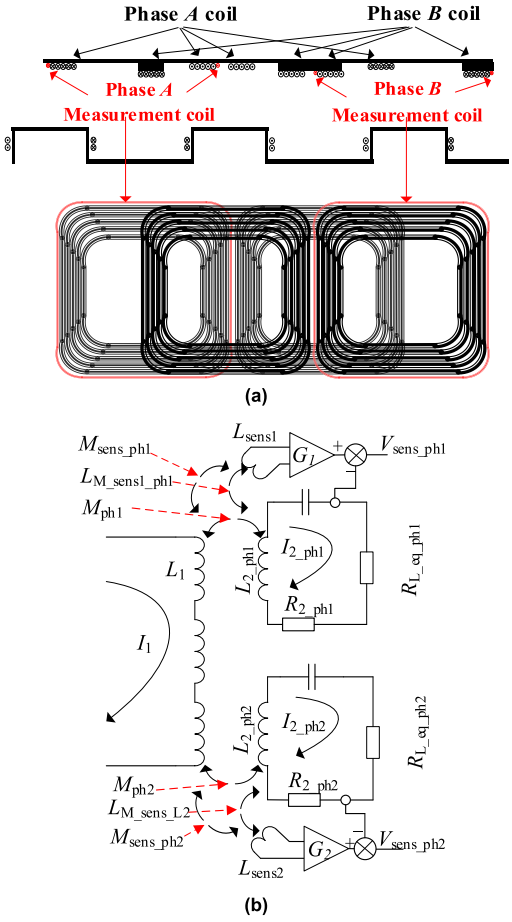

FIGURE 11. Model of auxiliary measurement coil for online estimation. (a) Coil structure (b) Circuit model.

TABLE 2. Notations in Fig. 11.

Notation	Description	Notation	Description
L_{sens1}	Self-inductance of Phase *A* auxiliary coil	L_{sens2}	Self-inductance of Phase *B* auxiliary coil
$M_{\text{sens\_ph1}}$	Mutual inductance of Phase *A* auxiliary coil and transmitter coil	$M_{\text{sens\_ph2}}$	Mutual inductance of Phase *B* auxiliary coil and transmitter coil
$L_{M\_\text{sens1\_ph1}}$	Mutual inductance of Phase *A* auxiliary coil and Phase *A* main coil	$L_{M\_\text{sens1\_ph2}}$	Mutual inductance of Phase *B* auxiliary coil and Phase *B* main coil
G_1	Gain of Phase *A* signal processor	G_2	Gain of Phase *B* signal processor

Through finite element analysis, $M_{\text{sens\_ph1}}$ and $M_{\text{sens\_ph2}}$ can be expressed as

$$\begin{cases} M_{\text{sens\_ph1}} = k_{\text{sens1\_max}}\sqrt{L_1 L_{\text{sens1}}}\left|\sin(\dfrac{\pi}{l}P_{\text{y}})\right| \\ M_{\text{sens\_ph2}} = k_{\text{sens2\_max}}\sqrt{L_1 L_{\text{sens2}}}\left|\sin(\dfrac{\pi}{l}P_{\text{y}}+\dfrac{\pi}{2})\right| \end{cases} \tag{29}$$

and the induced voltages in the measurement are

$$\begin{cases} V_{\text{ind\_sens\_ph1}} = j\omega I_1 k_{\text{sens1\_max}}\sqrt{L_1 L_{\text{sens1}}}\left|\sin(\dfrac{\pi}{l}P_{\text{y}})\right| \\ \quad +j\omega I_{2\_\text{ph1}} L_{\text{M\_sens1\_ph1}} \\ V_{\text{ind\_sens\_ph2}} = j\omega I_1 k_{\text{sens2\_max}}\sqrt{L_1 L_{\text{sens1}}}\left|\cos(\dfrac{\pi}{l}P_{\text{y}})\right| \\ \quad +j\omega I_{2\_\text{ph2}} L_{\text{M\_sens1\_ph2}} \end{cases} \tag{30}$$

Since there is no current passing through the measurement coil, the voltages at the measurement coils are $V_{\text{ind\_sens\_ph1}}$ and $V_{\text{ind\_sens\_ph2}}$. By detecting the receiver current and adjusting G_1 and G_2, the voltage in the measurement coil induced by the main coils of the receiver can be eliminated, so that $V_{\text{sens\_ph1}}$ and $V_{\text{sens\_ph2}}$, induced by the transmitter, can be extracted:

$$\begin{cases} V_{\text{sens\_ph1}} = jG_1\omega I_1 k_{\text{sens1\_max}}\sqrt{L_1 L_{\text{sens1}}}\left|\sin(\dfrac{\pi}{l}P_{\text{y}})\right| \\ V_{\text{sens\_ph2}} = jG_2\omega I_1 k_{\text{sens2\_max}}\sqrt{L_1 L_{\text{sens2}}}\left|\cos(\dfrac{\pi}{l}P_{\text{y}})\right| \end{cases} \tag{31}$$

where $k_{\text{sens1\_max}}$ and $k_{\text{sens2\_max}}$ are the maximum coupling coefficients between the measurement coil and the transmitter coil. By adjusting the size and position of the measurement coil and the G_1 and G_2, the expression can be achieved as

$$G_1\omega I_1 k_{\text{sens1\_max}}\sqrt{L_{\text{p}} L_{\text{sens1}}} = G_2\omega I_1 k_{\text{sens2\_max}}\sqrt{L_{\text{p}} L_{\text{sens2}}} \tag{32}$$

By calculating the ratio of $V_{\text{sens\_ph1}}$ to $V_{\text{sens\_ph2}}$, the relative position between the receiver and the transmitter is acquired:

$$\theta_{\text{posi}} = \frac{\pi}{l}P_{\text{y}} = \left|\arctan(\frac{V_{\text{sens\_ph1}}}{V_{\text{sens\_ph2}}})\right| \tag{33}$$

Then the distribution of the output currents of the two phases is available as

$$\begin{cases} \kappa = \sin^2\theta_{\text{posi}} = \sin^2\left(\left|\arctan(\dfrac{V_{\text{sens\_ph1}}}{V_{\text{sens\_ph2}}})\right|\right) \\ 1-\kappa = \cos^2\theta_{\text{posi}} = \cos^2\left(\left|\arctan(\dfrac{V_{\text{sens\_ph1}}}{V_{\text{sens\_ph2}}})\right|\right) \end{cases} \tag{34}$$

Finally, the output current of each phase can be computed as

$$\begin{cases} I_{o\_\text{ph1}} = \sin^2\left(\left|\arctan(\dfrac{V_{\text{sens\_ph1}}}{V_{\text{sens\_ph2}}})\right|\right) I_o \\ I_{o\_\text{ph2}} = \cos^2\left(\left|\arctan(\dfrac{V_{\text{sens\_ph1}}}{V_{\text{sens\_ph2}}})\right|\right) I_o \end{cases} \tag{35}$$

In the system controller, I_o is the target value of the total output current of the receiver, whereas the output current of each phase calculated by (35) should be used as the reference value of the output current of each phase.

The control strategy of the receiver is shown in detail in Fig. 12. With (a) being the first part of the controller, the relative position of the couplers θ_{posi} is acquired

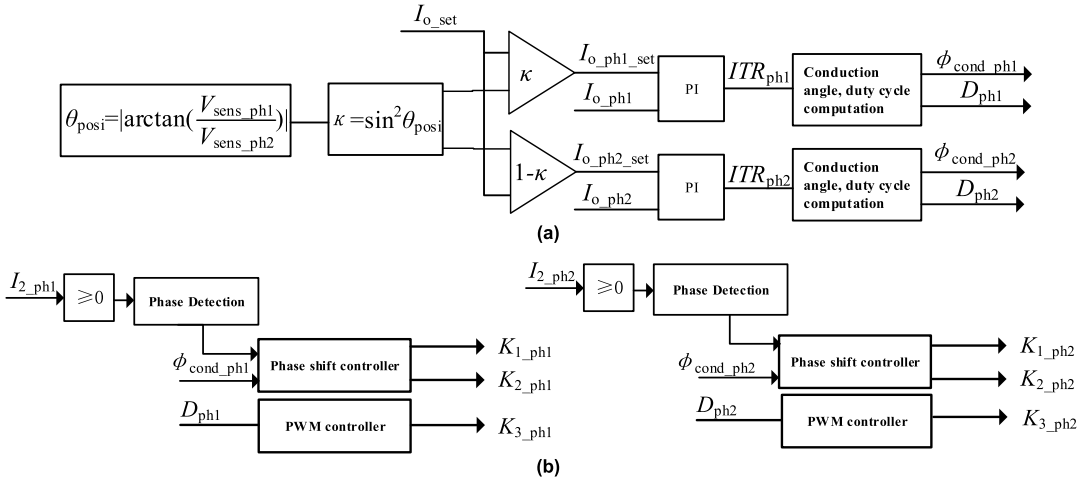

FIGURE 12. Control strategy of the receiver. (a) The control flow of the system controller (b) The control flow of the bridgeless rectifier and Buck controllers.

FIGURE 13. Dynamic charging experiment platform with two-phase receivers. (a) Transmitter and receivers (b) Impedance matching module.

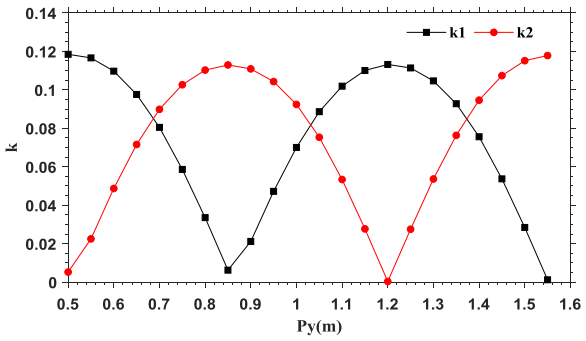

FIGURE 14. Coupling coefficient variations of the two phases in the experimental platform.

through output voltages of the auxiliary measurement circuits $V_{\text{sens\_ph1}}$ and $V_{\text{sens\_ph2}}$ and (33) entailed by the output current ratio of the two-phase receivers through (34). Setting the total output of the receiver a certain expected value, the current ratio can be used for the expected current $I_{\text{o\_set\_ph1}}$ and $I_{\text{o\_set\_ph2}}$ for each phase.

The control of the output current of each phase is accomplished by a PI controller, where the input is the detected output current and expected output current, and the output is *ITR* of the energy conversion topology. Based on (13) and the characteristics of Buck shown in TABLE 1, the output of the PI controller can be further converted to the conduction angle of the bridgeless rectifier and the duty cycle of the Buck circuit. The second part of the controller includes the phase shift controller of the bridgeless rectifier and the PWM controller of the Buck circuit. In order to ensure the synchronization

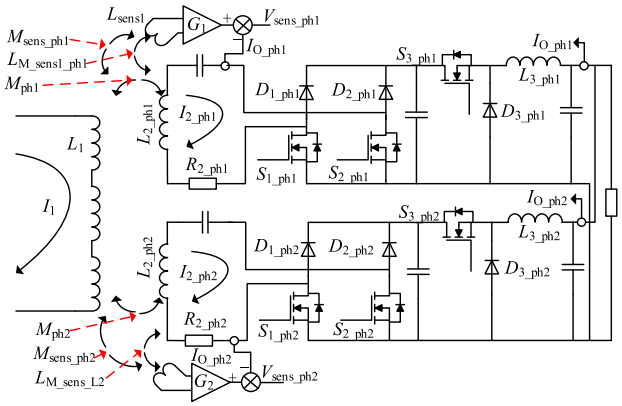

FIGURE 15. Circuitry of the receiver of the experimental platform.

of the input voltage and current of the rectifier, the phase of the resonant cavity of the receiver is required for the phase shift controller through current sensors. The controller then computes the phase and period of the current with stable square waves generated by comparators.

The Buke circuits use the fixed-frequency PWM controller in convenience for the selection of the filtering inductors and switching devices. In Fig. 12(b), $ITR_{\text{ph1,2}} = 1$ is set as the boundary for the computation of the conduction angle and duty cycle. When $ITR_{\text{ph1,2}} > 1$, the circuits work as an uncontrolled rectifier by shutting down the bridgeless rectifier. When $ITR_{\text{ph1,2}} < 1$, the duty cycle of Buck is set to 1. This control technique alternates the operation of the rectifier and Buck and reduces the switching losses.

V. EXPERIMENTS

In order to verify the feasibility of the topology and the control method proposed in this paper, a DWPT experimental platform with two-phase receivers is built (Fig. 13). This experimental system consists mainly of three parts: couplers including transmitter and receiver, bridgeless rectifier and impedance matching module of the receiver. The parameters of the couplers are shown in TABLE 3 and the variations of coupling coefficients are shown in Fig. 14. The schematic of the main circuit is shown in Fig. 15, where the switching devices are Infineon FF150R12KS4 high power IGBT models.

For the controller presented in Fig. 16, two cores (Cyclone IV EP4CE22F17I7N and ARM STM32F407) are chosen as the processors. Two high-speed AD channels are used to collect the currents in the two resonant cavities of the two-phase receivers so that the controller obtains the state variables through the digital integrator. The output signals of the auxiliary measurement coils are collected by ARM for the computation of the output ratio of the two phases after preprocessing. The ARM also handles PID control and other floating-point computation in the process. Closed-loop experiments are conducted at 20 kHz. The output current of the transmitter is set to 100 A, the total output current of the two-phase receivers is set to 40 A, and the load is 12.5 Ω.

TABLE 3. The parameters of couplers.

Parameters	Description	Value	Parameters	Description	Value
w	Width of the transmitter	100 mm	S_I	Inner size of the receiver	500 mm
d	Length of magnetic poles	300 mm	S_o	Outer size of the receiver	600 mm
l	Center distance of magnetic poles	600 mm	u	Width of single receiving coil	5 mm
H_1	Core thickness of the transmitter	10 mm	H_2	Core thickness of the receiver	10 mm
N_1	Coil turns of the transmitter	5	N_2	Coil turns of the receiver	12
L_1	Self-inductance of the transmitter	118.5 μH	L_2	Self-inductance of the receiver	950 μH
C_1	Resonant capacitor of the transmitter	533 nF	C_2	Resonant capacitor of the receiver	66 nF
R_1	AC resistance@20kHz of the transmitter	359 mΩ	R_2	AC resistance@20kHz of the receiver	512 mΩ

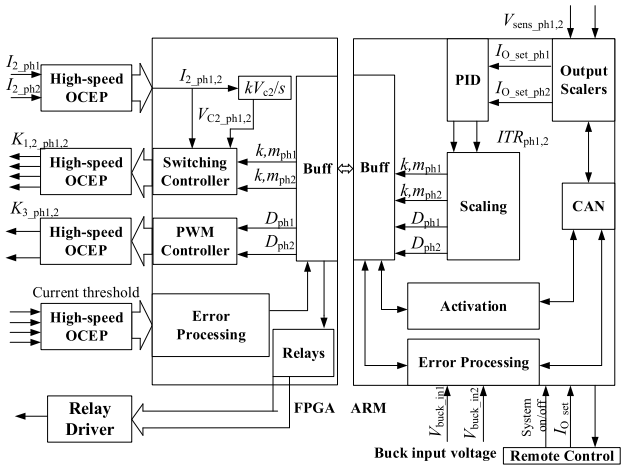

FIGURE 16. Schematics of the system controller.

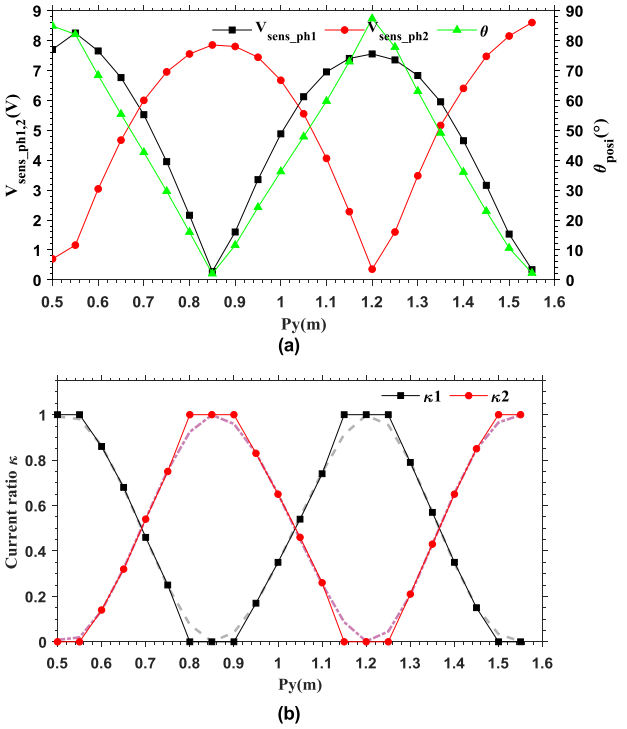

FIGURE 17. The experimental results related to the detection and control module. (a) Output voltages of the detection circuit and the current distribution angle (b) The output current ratio of each phase receiver.

Fig. 17 shows the experimental results related to the detection and control module of the proposed topology. The horizontal axis of the figures represents the distance. The receiver travels over the transmitter and the range is from 0.5 m∼1.5m which is more than twice the length of the magnetic poles of the transmitter. Fig. 17(a) shows the output voltages of the detection circuit reflecting the variations of the coupling coefficients, and the current distribution angle based on (33). Fig. 17(b) are the current ratios of the two phases in comparison with the calculated ones plotted in light dash lines according to the data in Fig. 17(a). The flat peak of the curve is because the controller would set the current ratio of the phase to 0 if it is less than 0.1, as described in the previous section.

Fig. 18 shows the results of the currents in the two-phase receivers and proves the feasibility of the system under constant current output conditions. Fig. 18(a) shows the output current of each phase and the total output current. The individual output current is consistent with the current ratio in Fig. 17(b), which fulfills the purpose of output current distribution for each phase according to the output voltages of the detection circuits. The total output current is close to constant satisfying the most fundamental condition and the assumption of the control method. Fig. 18(b) is the currents in the resonant cavities of the two-phase receivers entailed by the impedance transformation ratio of each phase (Fig. 18(c)) computed based on output currents and the resonant currents. The ITR is discontinuous because switching devices in Buck are off when the current ratio of the phase is 0.

To present the advantage of the proposed topology and control method, comparison in terms of transfer efficiency with conventional topology is made in Fig. 19, where the efficiency is measured every 5 cm along the transmitter as the other data. From the figure shown, the transfer efficiency is unambiguously improved by applying the new topology and controller method. The minimum efficiency is now 90.5% compared to 87.2% of the conventional topology and the maximum efficiency is 91.5% compared to 91.3%. The proposed topology can not only improve efficiency but also

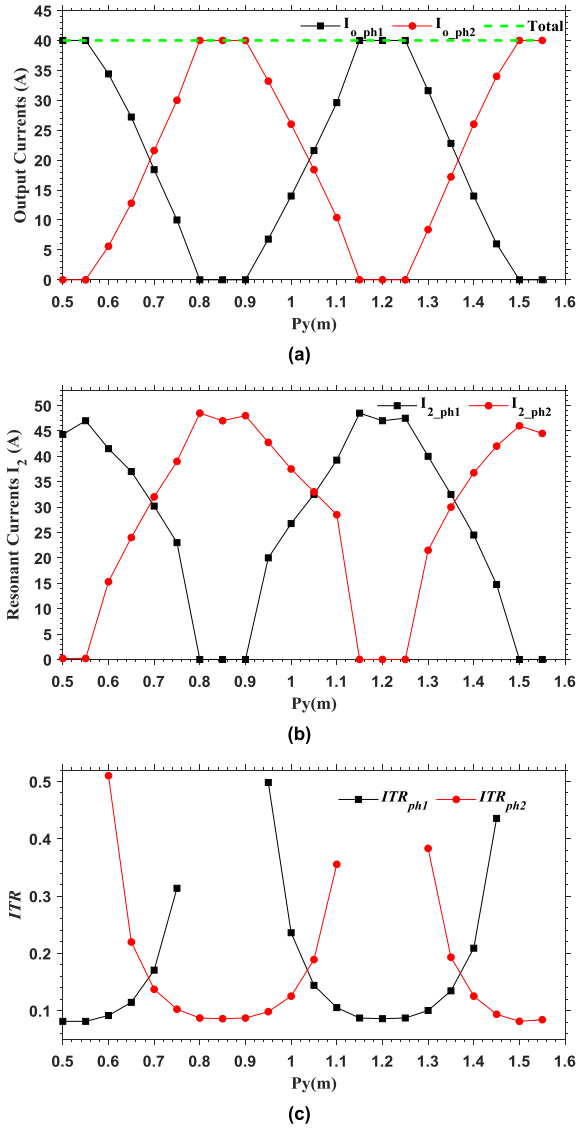

FIGURE 18. Experimental results of the output currents, resonant currents and impedance transformation ratio of each phase of (a) Phase output and total output current (b) Currents in the resonate cavities of the two-phase receivers. (c) Impedance transformation ratio *ITR*.

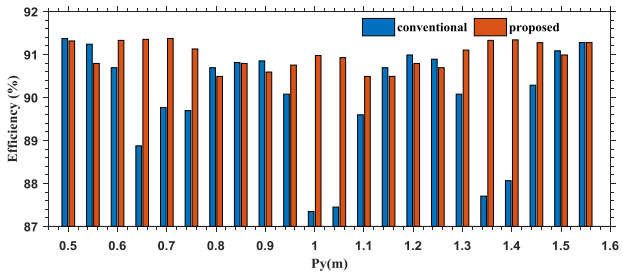

FIGURE 19. System efficiency comparison of conventional and proposed topologies.

smooth the "dents" in the efficiency curve during the entire operation as the vehicle moves along the transmitting rail indicating a better overall performance of the dynamic wireless charging system.

VI. CONCLUSION

Compared with the conventional topology of the two-phase receivers of the DWPT systems, the proposed topology is proved to improve two objectives: impedance matching range when constant current output is required and transfer efficiency as the vehicle moves along the power rail. With CBRB-based impedance matching structure, the range of impedance matching is broadened to $0\sim\infty\Omega$ without introducing more stages of DC-DC converters. And with the structure of independent two-channel impedance matching and its control method, the transfer efficiency is improved and maintained to a more steady level as the vehicle moves along the transmitter and the heuristic current ratio has great potential to reach the optimal efficiency. Experimental results also testify the feasibility and effectiveness of the proposed strategy.

REFERENCES

[1] M. Yilmaz and P. T. Krein, "Review of battery charger topologies, charging power levels, and infrastructure for plug-in electric and hybrid vehicles," *IEEE Trans. Power Electron.*, vol. 28, no. 5, pp. 2151–2169, May 2013.

[2] C. C. Mi, G. Buja, S. Y. Choi, and C. T. Rim, "Modern advances in wireless power transfer systems for roadway-powered electric vehicles," *IEEE Trans. Ind. Electron.*, vol. 63, no. 10, pp. 6533–6545, Oct. 2016.

[3] V.-B. Vu, V.-T. Phan, M. Dahidah, and V. Pickert, "Multiple output inductive charger for electric vehicles," *IEEE Trans. Power Electron.*, vol. 34, no. 8, pp. 7350–7368, Aug. 2019.

[4] S. Y. Choi and C. T. Rim, "Recent progress in developments of on-line electric vehicles," in *Proc. 6th Int. Conf. Power Electron. Syst. Appl. (PESA)*, Dec. 2015, pp. 1–8.

[5] O. C. Onar, J. M. Miller, S. L. Campbell, C. Coomer, C. P. White, and L. E. Seiber, "Oak ridge national laboratory wireless power transfer development for sustainable campus initiative," in *Proc. IEEE Transp. Electrific. Conf. Expo (ITEC)*, Jun. 2013, pp. 1–8.

[6] A. Foote and O. C. Onar, "A review of high-power wireless power transfer," in *Proc. IEEE Transp. Electrific. Conf. Expo (ITEC)*, Jun. 2017, pp. 234–240.

[7] C.-S. Wang, G. A. Covic, and O. H. Stielau, "Power transfer capability and bifurcation phenomena of loosely coupled inductive power transfer systems," *IEEE Trans. Ind. Electron.*, vol. 51, no. 1, pp. 148–157, Feb. 2004.

[8] C.-S. Wang, O. H. Stielau, and G. A. Covic, "Design considerations for a contactless electric vehicle battery charger," *IEEE Trans. Ind. Electron.*, vol. 52, no. 5, pp. 1308–1314, Oct. 2005.

[9] A. Zaheer, G. A. Covic, and D. Kacprzak, "A bipolar pad in a 10-kHz 300-W distributed IPT system for AGV applications," *IEEE Trans. Ind. Electron.*, vol. 61, no. 7, pp. 3288–3301, Jul. 2014.

[10] K. Hata, T. Imura, and Y. Hori, "Dynamic wireless power transfer system for electric vehicles to simplify ground facilities—Power control and efficiency maximization on the secondary side," in *Proc. 31st Annu. IEEE Appl. Power Electron. Conf. Expo. (APEC)*, Mar. 2016, pp. 1731–1736.

[11] J. M. Miller, P. T. Jones, J.-M. Li, and O. C. Onar, "ORNL experience and challenges facing dynamic wireless power charging of EV's," *IEEE Circuits Syst. Mag.*, vol. 15, no. 2, pp. 40–53, 2015.

[12] S. Y. Choi, B. W. Gu, S. Y. Jeong, and C. T. Rim, "Advances in wireless power transfer systems for roadway-powered electric vehicles," *IEEE J. Emerg. Sel. Topics Power Electron.*, vol. 3, no. 1, pp. 18–36, Mar. 2015.

[13] S. Y. Choi, S. Y. Jeong, B. W. Gu, G. C. Lim, and C. T. Rim, "Ultraslim S-type power supply rails for roadway-powered electric vehicles," *IEEE Trans. Power Electron.*, vol. 30, no. 11, pp. 6456–6468, Nov. 2015.

[14] C. Park, S. Lee, S. Y. Jeong, G.-H. Cho, and C. T. Rim, "Uniform power I-type inductive power transfer system with DQ-power supply rails for on-line electric vehicles," *IEEE Trans. Power Electron.*, vol. 30, no. 11, pp. 6446–6455, Nov. 2015.

[15] K. Hata, T. Imura, and Y. Hori, "Maximum efficiency control of wireless power transfer via magnetic resonant coupling considering dynamics of DC-DC converter for moving electric vehicles," in *Proc. IEEE Appl. Power Electron. Conf. Exposit. (APEC)*, Mar. 2015, pp. 3301–3306.

[16] A. Zaheer, M. Neath, H. Z. Z. Beh, and G. A. Covic, "A dynamic EV charging system for slow moving traffic applications," *IEEE Trans. Transport. Electrific.*, vol. 3, no. 2, pp. 354–369, Jun. 2017.
[17] R. Mai, Y. Liu, Y. Li, P. Yue, G. Cao, and Z. He, "An active-rectifier-based maximum efficiency tracking method using an additional measurement coil for wireless power transfer," *IEEE Trans. Power Electron.*, vol. 33, no. 1, pp. 716–728, Jan. 2018.
[18] S. Cui, Z. Wang, S. Han, C. Zhu, and C. C. Chan, "Analysis and design of multiphase receiver with reduction of output fluctuation for EV dynamic wireless charging system," *IEEE Trans. Power Electron.*, vol. 34, no. 5, pp. 4112–4124, May 2019.
[19] Z. Li, K. Song, J. Jiang, and C. Zhu, "Constant current charging and maximum efficiency tracking control scheme for supercapacitor wireless charging," *IEEE Trans. Power Electron.*, vol. 33, no. 10, pp. 9088–9100, Oct. 2018.
[20] K. Song, Z. Li, J. Jiang, and C. Zhu, "Constant current/voltage charging operation for series-series and series-parallel compensated wireless power transfer systems employing primary-side controller," *IEEE Trans. Power Electron.*, vol. 33, no. 9, pp. 8065–8080, Sep. 2017.

JINHAI JIANG received the B.S. and M.S. degrees from the School of Electrical Engineering and Information, Northeast Petroleum University, Daqing, China, in 2010 and 2013, respectively, and the Ph.D. degree in electrical engineering from the Harbin Institute of Technology (HIT), Harbin, China, in 2019.

He is currently a Lecturer with the School of Electrical Engineering & Automation, HIT. His research interest includes wireless power transfer for super-capacitor and battery-powered online electric vehicles.

ZHONGGANG LI is currently pursuing the B.S. degree with the School of Instrumentation Science and Engineering, Harbin Institute of Technology (HIT), Harbin, China.

His research interest includes wireless power transfer for on-line electric vehicles and automatic guided vehicles (AGV).

KAI SONG (Senior Member, IEEE) received the B.S. and Ph.D. degrees in electrical engineering and automation from the Harbin Institute of Technology (HIT), Harbin, China, in 2005 and 2011, respectively.

In 2011, he joined the School of Electrical Engineering and Automation, HIT, as a Lecturer. He was a Visiting Scholar of electrical engineering with The University of Tokyo, Japan, from 2014 to 2015. He is currently an Associate Professor with HIT, where he has been the Deputy Director of the Institute of Wireless Power Transfer Technology, since 2016. He has coauthored more than 60 peer-reviewed technical articles and authorized 30 invention patents in China. His current research interest includes wireless power transfer, particularly in wireless charging systems for electric vehicles.

BEIBEI SONG received the B.S. and M.S. degrees with the School of Electrical Engineering and Automation from the Harbin Institute of Technology (HIT), Harbin, China, in 2016 and 2018, respectively. He is currently pursuing the Ph.D. degree.

His research interest includes wireless power transfer and dynamic wireless charging for electric vehicles

SHUAI DONG received the M.S. and Ph.D. degrees in electrical engineering from the Harbin Institute of Technology (HIT), Harbin, China, in 2011 and 2016, respectively.

He has been a Lecturer with the School of Electrical Engineering and Automation, HIT, since 2017. He specializes in the research field of wireless power transfer and power electronics for electric vehicle applications.

CHUNBO ZHU (Member, IEEE) received the B.S. and M.S. degrees in electrical engineering and the Ph.D. degree in mechanical engineering from the Harbin Institute of Technology (HIT), Harbin, China, in 1987, 1992, and 2001, respectively.

He was a Postdoctoral Research Fellow with the PEI Research Center, National University of Ireland, Galway, Ireland, from 2003 to 2004. He has been a Lecturer with the Department of Automation Measurement and Control, HIT, since 1987. He is currently a Full Professor with HIT, where he leads the Laboratory of Wireless Power Transfer and Battery Management Technologies. His current research interests include energy management systems, electric and hybrid electric vehicles, and wireless power transfer technologies.